Proceedings of the Thirty-fifth (2025) International Ocean and Polar Engineering Conference **www.isope.org**
Seoul/Goyang, Korea, June 1-6, 2025

ISBN 978-1-880653-74-6; ISSN 1098-6189

Effect of elastic properties of sediment on sound pressure kurtosis for marine airgun signal

Yaxi Peng, Apostolos Tsouvalas
Department of Hydraulic Engineering, Faculty of Civil Engineering and Geosciences, Delft University of Technology
Delft, South Holland, Netherlands

Ozkan Sertlek
JASCO Applied Sciences, Schwentinental, Germany

ABSTRACT

Seismic airguns are widely used in offshore environments to investigate sub-seafloor layers, generating intense, impulsive sound waves that propagate through seawater, penetrate the seabed, and travel tens to hundreds of kilometers from the source. The characteristics of these acoustic waves evolve as they interact with sediment layers and the sea surface, which can alter the temporal features of the sound pressure reaching marine life at various distances. Assessing sound pressure wave properties across different environments is essential for selecting metrics that effectively gauge the impact of seismic noise on aquatic ecosystems. One such metric, sound pressure kurtosis, reflects the impulsive nature of sound waves and provides a measure of their impulsiveness, which is particularly relevant for assessing potential effects on marine animals. In this study, Green's functions for the acousto-elastodynamic problem are employed to model sound propagation from seismic airguns, capturing the influence of the seafloor's elastic properties on sound dispersion. We investigate variations in sound pressure kurtosis across various sediment types, including sandy, silty, and clay-like substrates, examining how each affects the impulsive characteristics of airgun-generated pulses. Additionally, the temporal dispersion of pressure signals from individual airgun shots is analyzed as they interact with differing marine sediments, providing insights into the impact of the seafloor's elastic properties on sound emissions affecting marine life.

KEY WORDS: Seismic airgun, Green's function, Sound Pressure Kurtosis, elastic properties, marine life.

INTRODUCTION

Anthropogenic underwater noise poses a significant threat to aquatic life, raising growing concerns about its adverse effects. Among various human-made activities, marine airgun operations, widely employed for seismic surveys, generate extremely high levels of impulsive underwater sound and are considered one of the most impactful noise sources endangering marine ecosystems (Slabbekoorn et al., 2019; Sidorovskaia and Li, 2022; Lucke et al., 2024).

During these operations, explosive sounds are produced by an array of airguns towed behind a survey vessel. When the airguns are fired in synchronization, intense echoes are generated from deep penetrations into marine sediments and multiple reflections from the sea surface and ocean bottom. The recorded acoustic signals are then analyzed to map the substructure of the seafloor, aiding oil and gas exploration. These airgun pulses are typically repeated over periods lasting up to several months, with intervals ranging from 4 to 20 seconds between each shot. There is considerable interest in understanding the impact of airgun noise on marine species. Numerous studies have been conducted to investigate the characteristics of seismic airgun pulses and their propagation in the marine environment (Sertlek et al., 2024). To evaluate the effects of anthropogenic noise on different marine species, various noise thresholds have been proposed.

Exposures exceeding these thresholds can potentially cause auditory injuries, such as temporary threshold shifts (TTS) and permanent threshold shifts (PTS), in marine mammals (Southall et al., 2019). However, assessing the effects of anthropogenic noise on fish, invertebrates, crustaceans, and marine mammals can be challenging. Beyond exposure and peak pressure levels, other factors—such as exposure frequency, duration, and the spatial and temporal patterns of sound pressure—are critical to impact assessments. Research indicates that the hearing organs of marine animals are particularly vulnerable to injury from impulsive sounds. Metrics like the sound pressure kurtosis index, which are sensitive to the impulsive nature of sound, should be considered for more accurate assessments.

Recent work by Sertlek et al. (2024) analyzed the effects of sediment type and range on the time dispersion of sound signals from a single airgun shot using an equivalent fluid model. However, this approach does not fully capture the elastic properties of marine sediments, which can significantly influence sound propagation. Addressing this gap, the present study extends the investigation by examining sound pressure

kurtosis across various sediment types, incorporating their elastic characteristics.

To achieve this, Green's functions for the acousto-elastodynamic problem are employed, allowing for a more comprehensive modeling of sound propagation from seismic airguns. This approach accounts for the influence of seafloor elasticity on sound dispersion, which has been largely overlooked in previous studies. By evaluating variations in marine sediment properties, this study assesses their impact on the impulsive characteristics of airgun-generated pulses. Additionally, the temporal dispersion of pressure signals from individual airgun shots is analyzed, providing new insights into how environmental factors shape airgun pulses during propagation.

This article is organized as follows: The section on sound propagation modeling describes the propagation model in detail, including the mathematical methodology, the source characterization and kurtosis calculations. The next section focuses on simulations based on a shallow-water test case from the JIP Acoustic Modelling (JAM) Workshop, held in Cambridge, UK, in 2022 (Ainslie et al., 2024). Various sediment types, including those with elastic properties, are examined. The final section presents the discussion and conclusions.

SILENCE PROPAGATION MODEL

To calculate the sound pressure kurtosis, it is necessary to determine the sound pressure in the time domain at various horizontal distances from the airgun source. For this study, the SILENCE model, which accounts for the effects of a layered elastic sediment, is utilized (Peng et al., 2021). The SILENCE model is based on the complex wave number integration method and was originally developed to model sound propagation from offshore pile driving over a wide frequency spectrum. This model can generate responses in both fluid and sediment domains, including pressure, velocity, displacement, and stress fields. This section describes the detailed derivations of SILENCE propagation model including the elastic description of the marine sediment as depicted in Fig. 1. The derivation is generalised for marine sediment consists of horizontal stratified layers.

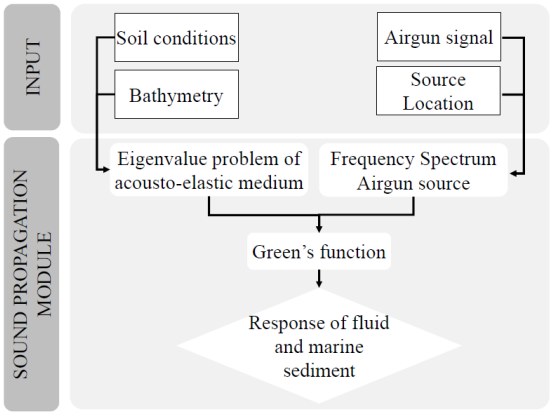

Fig. 1 Activity flow of the SILENCE propagation model.

The model is used to calculate propagation loss for a point source in an acousto-elastic waveguide, incorporating elastic sediment properties to address the test cases presented in Fig. 2 from the JAM Workshop (Ainslie et al., 2024). The pressure field in the ocean environment is represented as a finite sum of modes and a complex wavenumber integral, utilizing the Ewing–Jardetzky–Press (EJP) cut. This solution is extended from the case of two fluid layers to a scenario involving a fluid layer overlying a solid half-space, as outlined in Peng et al. (2021). The accuracy of the SILENCE model has been verified in Peng et al. (2021) and Sertlek et al. (2024) by comparing the propagation loss (PL) results with those from other well-established propagation models for a bench mark case.

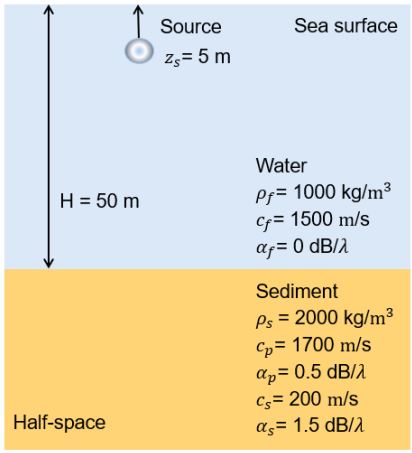

Fig. 2 Geometry of the model. Adapted from Fig. 1 of Ainslie et al. (2024).

Governing equations

The following partial differential equations govern the dynamic response of the acousto-elastic media in time domain:

$$\nabla^2 p_f(r,z,t) - \frac{1}{c_f^2}\ddot{p}_f(r,z,t) = 0\,, \tag{1}$$

$$(\lambda_j + 2\mu_j)\nabla(\nabla\cdot\mathbf{u}_j) - \mu_j\nabla\times(\nabla\times\mathbf{u}_j) = \rho_j\ddot{\mathbf{u}}_j. \tag{2}$$

In Eq. (1), $p_f(r,z,t)$ is the pressure field of the fluid. In Eq. (2), $\mathbf{u}_j = [w_j(r,z,t)\ u_j(r,z,t)]^{\mathrm{T}}$ is the vertical and radial displacements of soil layer j.
The Helmholtz decomposition can be applied to the fluid-soil domain as:

$$\mathbf{u}_f = \nabla\phi_f, \quad \mathbf{u}_j = \nabla\phi_j + \nabla\times(0, -\frac{\partial\psi_j}{\partial r}, 0) \tag{3}$$

Substitution of Eq. (3) into Eqs. (1) and (2) yields:

$$\nabla^2\phi_f(r,z,t) = \frac{1}{c_f^2}\frac{\partial^2\phi_f}{\partial t^2}\,, \tag{4}$$

$$\nabla^2\phi_j(r,z,t) = \frac{1}{c_{p_j}^2}\frac{\partial^2\phi_j}{\partial t^2}\,, \tag{5}$$

$$\nabla^2\psi_j(r,z,t) = \frac{1}{c_{s_j}^2}\frac{\partial^2\psi_j}{\partial t^2}\,. \tag{6}$$

In the equations above, c_{p_j} and c_{s_j} denote the speeds of the compressional and shear waves in soil layer j, respectively. The pressure release boundary condition is applied at the sea surface. At the fluid-soil interface $z = z_1$, the vertical stress equilibrium and the vertical displacement continuity are imposed, while the shear stress vanishes since no tangential stresses present in a perfect fluid. The bottom soil is extended to infinity to mimic realistic ocean environments. Given the full-contact at the soil-soil interface, both stress equilibrium and displacement continu-

ity are applied. This set of boundary and interface conditions reads:

$$p_f(r, z_0, t) = 0, \quad r \geq R, \tag{7}$$

$$\sigma_{zz_1}(r, z_1, t) + p_f(r, z_1, t) = 0, \quad u_{z,f}(r, z_1, t) = w_{s_1}(r, z_1, t), \tag{8}$$

$$\sigma_{zr_1}(r, z_1, t) = 0, \quad r \geq R, \tag{9}$$

$$w_j(r, z_j, t) = w_{j-1}(r, z_j, t), \quad u_j(r, z_j, t) = u_{j-1}(r, z_j, t), \tag{10}$$

$$2 \leq j \leq N, \quad r \geq R, \tag{11}$$

$$\sigma_{zz_j}(r, z_j, t) = \sigma_{zz_{j-1}}(r, z_j, t), \quad \sigma_{zr_j}(r, z_j, t) = \sigma_{zr_{j-1}}(r, z_j, t), \tag{12}$$

$$2 \leq j \leq N, \quad r \geq R. \tag{13}$$

In Eq. (13), σ_{zz_j} and σ_{zr_j} designate the normal and tangential stresses in the soil layer j.

After applying the forward Fourier transform, the governing equations in frequency domain are obtained. The Fourier transform pair used in this paper is expressed as:

$$g(t) = \frac{1}{2\pi} \int_{-\infty}^{+\infty} \widetilde{G}(\omega) e^{\mathrm{i}\omega t} d\omega \quad \text{and} \quad \widetilde{G}(\omega) = \int_{-\infty}^{+\infty} g(t) e^{-\mathrm{i}\omega t} dt \tag{14}$$

in which $g(t)$ and $\widetilde{G}(\omega)$ denote the physical quantities in the time and frequency domains, respectively.

Green's function

In this section, the Green's function solution for a point source located in a fluid within an acousto-elastic half-space is derived. The Hankel transform and complex contour integration approach are used to obtain a closed-form response in the frequency domain. The Hankel transform pair is given as:

$$\hat{f}(k_r) = \int_0^{\infty} f(r) J_0(k_r r) r dr \quad \text{and} \quad f(r) = \int_0^{\infty} \hat{f}(k_r) J_0(k_r r) k_r dk_r \tag{15}$$

in which $f(r)$ and $\hat{f}(k_r)$ denote the functions in the frequency domain and Hankel domain, respectively. $J_0(k_r r)$ is the Bessel function of the first kind of order zero and k_r is the horizontal wavenumber of the medium. To derive the Green's functions for an acoustic source, a pressure-type point source is placed at $[0, z_s]$ in the fluid domain, which generates pressure waves and produces a unit pressure amplitude at the location of the source. The equation of motion for the displacement potential reads:

$$[\nabla^2 + k_f^2] \tilde{\phi}^g_{f,f}(r, z; 0, z_s, \omega) = \frac{1}{-\rho\omega^2} \frac{\delta(r - 0, z - z_s)}{2\pi r}, \quad z_0 \leq z_s \leq z_1 \tag{16}$$

in which the first subscript of the Green's potential function denotes the location of the receiver, and the second subscript denotes the location of the source with "f" being the fluid domain. The homogeneous equations of motion for the displacement potentials $\phi_{s,f}$ and $\psi_{s,f}$ in the soil are given by Eqs. (5) and (6). Applying the forward Hankel transform to Eqs. (5), (6) and (16), the wave equations are reduced to depth-separated wave equations in the Hankel domain.

$$\left[\frac{d^2}{dz^2} + k_{z,f}^2\right] \hat{\phi}^g_{f,f}(k_r, z; 0, z_s, \omega) = \frac{1}{-\rho\omega^2} \frac{\delta(z - z_s)}{2\pi}, \tag{17}$$

$$\left[\frac{d^2}{dz^2} + k_{z,p_j}^2\right] \hat{\phi}^g_{j,f}(k_r, z; 0, z_s, \omega) = 0, \tag{18}$$

$$\left[\frac{d^2}{dz^2} + k_{z,s_j}^2\right] \hat{\psi}^g_{j,f}(k_r, z; 0, z_s, \omega) = 0. \tag{19}$$

in which $k_{z,\xi} = \sqrt{k_\xi^2 - k_r^2}$ is the vertical wavenumber in the domain ξ ($=f, p_j$ or s_j). The boundary conditions of the acousto-elastic medium

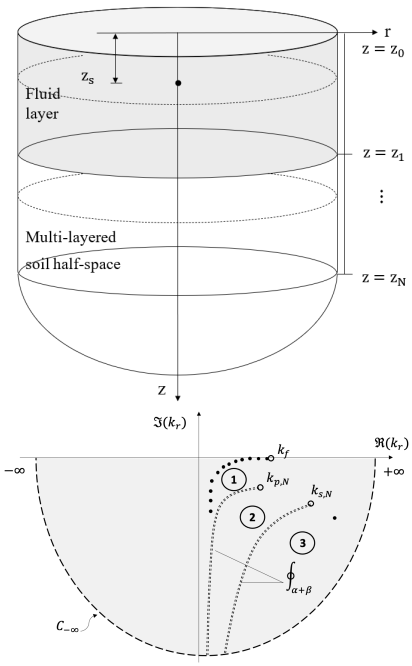

Fig. 3 Schematic representation of an acousto-elastic layered half-space with a point source positioned in the water (top) and visualization of the complex wavenumber integration approach (bottom).

along the z-coordinate have been specified in Eqs. (7)-(13).

The solutions for the displacement potentials are the sum of a particular solution and the general solution to the homogeneous equation:

$$\hat{\phi}^g_{f,f}(k_r, z; r_s, z_s, \omega) = \left(\frac{1}{-\rho\omega^2} \frac{e^{-\mathrm{i}k_{z,f}|z - z_s|}}{4\pi \mathrm{i} k_{z,f}} + A_1^g e^{\mathrm{i}k_{z,f} z} + A_2^g e^{-\mathrm{i}k_{z,f} z}\right) J_0(k_r r_s), \tag{20}$$

$$\hat{\phi}^g_{j,f}(k_r, z; r_s, z_s, \omega) = \left(A^g_{4j-1} e^{\mathrm{i}k_{z,p_j} z} + A^g_{4j} e^{-\mathrm{i}k_{z,p_j} z}\right) J_0(k_r r_s), \tag{21}$$

$$\hat{\psi}^g_{j,f}(k_r, z; r_s, z_s, \omega) = \left(A^g_{4j+1} e^{\mathrm{i}k_{z,s_j} z} + A^g_{4j+2} e^{-\mathrm{i}k_{z,s_j} z}\right) J_0(k_r r_s). \tag{22}$$

in which the coefficients A_i^g ($i = 1, 2, ..., 4N + 2$) are undetermined complex amplitudes. Two unknown amplitude coefficients in the potential function ϕ_f indicating upward- and downward- propagating waves in the fluid, four unknown amplitude coefficients in the functions ϕ_s and ψ_s indicating upward- and downward-propagating waves in each soil layer. When $j = N$, the amplitudes in front of the first term in both Eqs. (21) and (22) vanish to ensure the radiation condition at infinity in z direction.

Applying the inverse Hankel transform with the use of the relationships of the Bessel functions, the Green's tensor of the acousto-elastic medium in the frequency domain is obtained as:

$$\tilde{\mathbf{\Phi}}^g_{\Xi,f}(r, z; r_s, z_s, \omega) = -\frac{1}{2} \int_{-\infty}^{+\infty} \left(\hat{\mathbf{\Phi}}^g_{\Xi,f}(k_r, z; r_s, z_s, \omega)\right) H_0^{(2)}(k_r r) k_r dk_r \tag{23}$$

in which $\hat{\mathbf{\Phi}}^g_{\Xi,f} = [\hat{\phi}^g_{f,f}, \hat{\phi}^g_{j,f}, \hat{\psi}^g_{j,f}]^{\mathrm{T}}$ denotes the solutions of displacement potential functions in Hankel domain, $\tilde{\mathbf{\Phi}}^g_{\Xi,f}$ are the corresponding potential functions in frequency domain. The pressure, displacements and stresses of the acousto-elastic medium are expressed by the Green's functions of displacement potentials, which are omitted here for the

sake of brevity. By substituting the expressions into the boundary and interface conditions, the final set of linear algebraic equations with unknowns A_i^g for $i = 1, 2, ..., 4N + 2$ is obtained. Once the amplitude coefficients are solved for every k_r, the Green's tensor for a pressure-type point source placed in the fluid domain is obtained.

The evaluation of the integrals given by Eq. (23) can be achieved by using the contour integration technique, which is basically the *normal mode* method enriched with the branch line integration as depicted in Fig. 3 (bottom). The integral along the real axis can be expressed as:

$$\int_{-\infty}^{+\infty} f(k_r)dk_r = -2\pi \mathrm{i} \sum_{m=1}^{M} \mathrm{Res}(k_r^{(m)}) + \int_{\alpha+\beta} \tag{24}$$

in which $\mathrm{Res}(f(k_r), k_r^{(m)})$ is the residue of a general function $f(k_r)$ to a simple pole at $k_r = k_r^{(m)}$.

By applying the complex contour integration technique, the expressions of displacement potential functions in frequency domain are given as a summation over a finite number of poles supplemented by the Ewing-Jardetsky-Press (EJP) branch line integrations, i.e. :

$$\begin{aligned}\widetilde{\mathbf{\Phi}}^g_{\Xi,\xi}(r, z; r_s, z_s; \omega) = -\pi i \sum_{m=1}^{M} \Big[\mathrm{Res}(\hat{\mathbf{\Phi}}^g_{\Xi,\xi}(k_r^{(m)}, z; r_s, z_s)) H_0^{(2)}(k_r^{(m)} r) k_r^{(m)}\Big] \\ + \frac{1}{2} \int_{\alpha+\beta} \hat{\mathbf{\Phi}}^g_{\Xi,\xi}(k_r, z; r_s, z_s) H_0^{(2)}(k_r r) k_r dk_r\end{aligned} \tag{25}$$

As shown in Fig. 3, the EJP branch cuts are given in two hyperbolic lines starting from the branch points, which are the medium wavenumbers corresponding to compressional and shear waves. The full solutions consist of three terms: a) a finite sum of discrete modes on the principle Riemann surface (can be infinite in the case of the fluid layer overlying multi-layered elastic half-space), in which all modes are convergent; b) a hyperbolic branch line integration associated with the branch point of compressional wavenumber k_p; c) a hyperbolic branch line integration associated with the branch point of shear wavenumber k_s. The above solutions provide the basis of the sound propagation model.

Airgun source signature

Airgun source signatures can be estimated using various multi-physics models to describe the sound generated by the release of highly compressed bubbles from an airgun or airgun arrays. Marine airgun modeling workshops were held in Dublin, Ireland, in 2016 (Ainslie et al., 2019) and in Cambridge, UK, in 2022 (Ainslie et al., 2024). At both workshops, the source signature of a single airgun was examined as a reference case. The time-domain source waveform and frequency spectrum for this source signature are shown in Fig. 4. For the present study, the same reference case is considered, utilizing the airgun source waveform.

Calculation of kurtosis

The general statistical definition of kurtosis relates to the degree of heaviness in the tails of a statistical random variable or the distribution of sample values. In the context of a sound pressure time series, kurtosis follows the same definition, describing the distribution of pressure values. It is independent of the temporal structure of the signal and the scaling of its amplitude. To resolve the ambiguity surrounding the term "impulsive signal" and to provide clearer characterizations, Muller et al. (2020) analyzed sound pressure field in time using kurtosis. The sound pressure kurtosis, denoted as β, is calculated as follows:

$$\beta = \frac{\mu_4}{\mu_2^2} \tag{26}$$

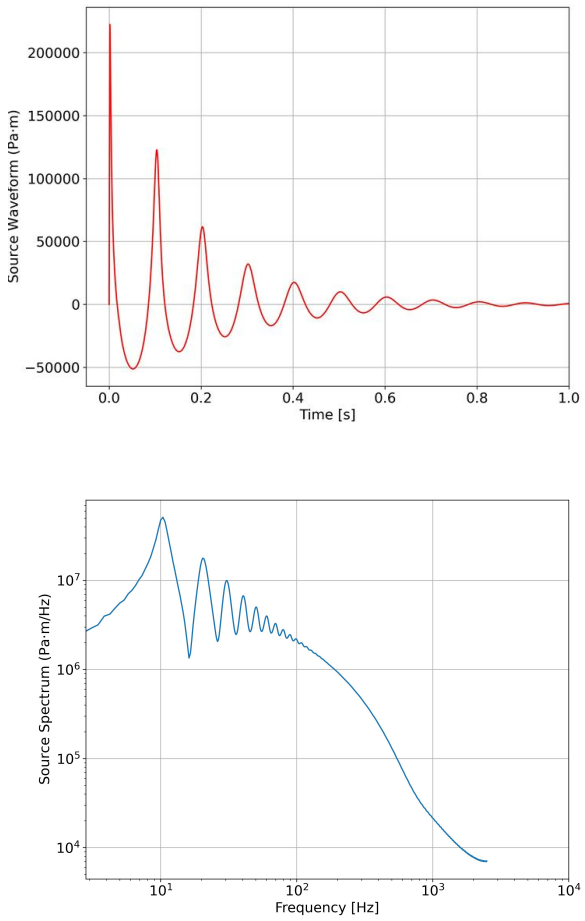

Fig. 4 Airgun source signature (top) and spectrum (bottom).

where μ_4 and μ_2 is the sound pressure variance defined as below,

$$\mu_4 = \frac{1}{t_1 - t_0} \int_{t_0}^{t_1} [p(t) - \bar{p}]^4 \tag{27}$$

$$\mu_2 = \frac{1}{t_1 - t_0} \int_{t_0}^{t_1} [p(t) - \bar{p}]^2 \tag{28}$$

where $p(t)$ is sound pressure, $\bar{p}$ is mean sound pressure, and t_0 and t_1 are the time points where the signal starts and ends, as described in ISO 18405:2017 (ISO, 2017).

NUMERICAL RESULTS

In this section, sound pressure kurtosis is calculated for several sediment types, including sandy, silt and clay-like substrates, as well as the workshop reference case. The influence of sediment type on the impulsive characteristics of airgun-generated pulses is analyzed. The geometry of the case study is depicted in Fig.2, where the marine airgun source is positioned 5 m below the sea surface, and the receiver is located at a depth of 15 m. The airgun signature at the source is shown in Fig. 4. The sound pressure is analyzed up to a distance of 3 km. The material properties of the marine sediments are provided in Table 1. These properties include representative grain size, density, compressional and shear wave sound speeds, and absorption coefficients for both wave types, as detailed in Ainslie (2010).

Table 1 Properties of the sediment types. The sound speed in water is 1500 m/s, and density is 1000 kg/m^3.

Sediment type	Representative grain size ϕ	ρ [kg/m^3]	C_p [m/s]	C_s [m/s]	α_p [dB/λ]	α_s [dB/λ]
Coarse sand	0.5	2231	1875	353	0.87	7.88
Medium sand	1.5	2086	1797	319	0.88	7.88
Fine sand	2.5	1945	1730	295	0.89	7.88
Workshop case	-	2000	1700	334	0.5	4.00
Very fine sand	3.5	1817	1670	280	0.49	4.00
Coarse silt	4.5	1702	1615	269	1.22	5.29
Medium silt	5.5	1601	1570	340	0.38	5.29
Fine silt	6.5	1513	1535	205	0.17	5.29
Very fine silt	7.5	1439	1510	108	0.11	5.29
Coarse Clay	8.5	1378	1490	50	0.08	18.95
Medium Clay	9.5	1331	1470	30	0.09	18.95

Comparison to equivalent fluid model

Based on the workshop case, the time dispersion calculated using the two SILENCE propagation models—one with an equivalent fluid sediment and the other modeling the seabed as an elastic medium—is presented in Fig. 5. The SILENCE-fluid model employs the same complex wavenumber integration method for simulating sound propagation from an airgun array. Its mathematical formulation has been discussed by Sertlek et al. (2024). The waveform for the workshop case, incorporating sediment elasticity, is computed using SILENCE-elastic.

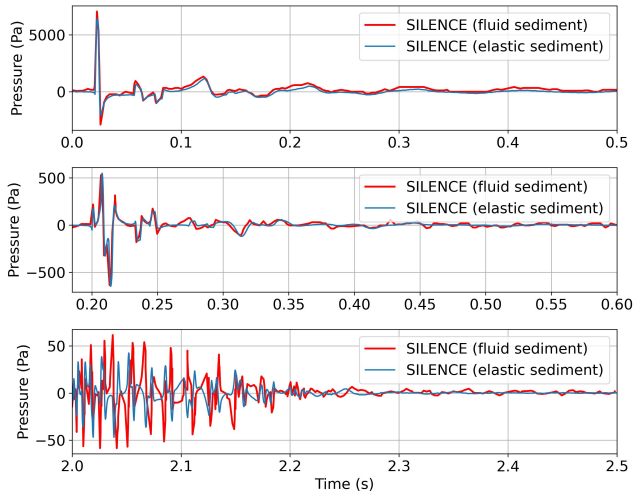

Fig. 5 Comparison of Time-Domain Waveforms Calculated Using SILENCE-elastic and SILENCE-fluid Propagation Models with Elastic Sediment Properties. Sound Pressure vs. Time at Ranges of 30 m (Top), 300 m (Middle), and 3000 m (Bottom).

The pressure fields at 30 m and 300 m from the single airgun source show good agreement between both models. However, at a range of 3000 m, the waveforms exhibit significant differences in shape and amplitude, despite both having a similar total pulse duration of 0.2 s. Since the source is located in the water column, most energy is carried by the primary water-borne transmission path. As a result, the near-field pressure waveforms remain relatively consistent between the two SILENCE models. At greater propagation distances, energy is increasingly radiated into compressional and shear waves due to multiple reflections and refractions at the fluid-sediment interface. In the ocean environment, shear waves are commonly higher attenuation than the compressional waves, leading to a lower pressure amplitude when the seabed is modeled as an elastic medium with attenuation.

Kurtosis

The sound kurtosis is calculated for different sediment types, as indicated in Table 1. The pressure waveforms are first computed over a total duration of 10 s. Ambient noise is incorporated by adding Gaussian noise with an RMS value of 1 Pa as shown in Fig. 6, assuming a background noise level of 120 dB SPL, resulting in a more realistic kurtosis estimation.

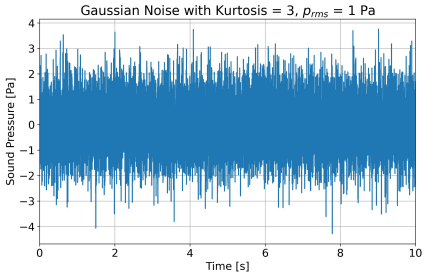

Fig. 6 Gaussian noise with rms sound pressure of 1 Pa

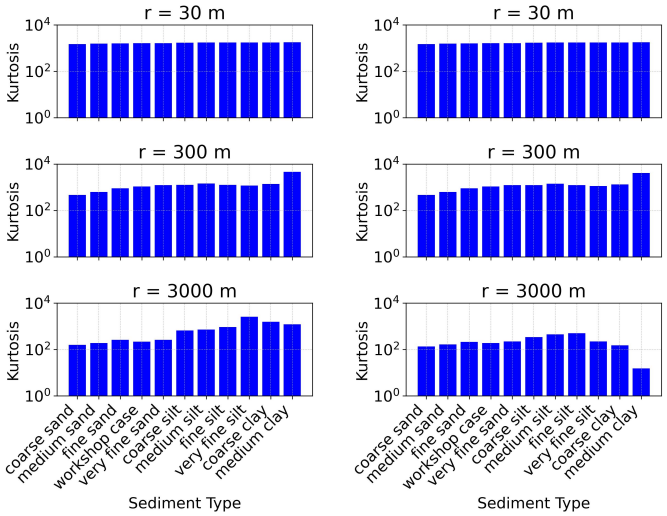

Fig. 7 Kurtosis with (right) and without (left) additional Gaussian noise at 30 m, 300 m, and 3000 m for different sediment types. T = 10 s.

Similar to observations from SILENCE (equivalent fluid model), kurtosis follows a similar trend at shorter ranges (30 m and 300 m) as shown in Fig. 7. However, as the observation point moves farther away, kurtosis levels are significantly higher for silt- and clay-like sediments compared to those computed using the equivalent fluid model. In the equivalent fluid model, kurtosis values for silt and clay are much lower, approaching the Gaussian noise level ($\beta = 3$). For these sediments, compressional wave speeds are considerably lower than in sandy substrates. When mod-

eling the seabed as an acoustic domain, a larger portion of energy radiates into the acoustic half-space, resulting in weaker reflections at the water-sediment interface. In contrast, when the sediment is modeled as an elastic medium, wave reflections and refractions at the water-sediment interface are better captured, leading to more realistic kurtosis levels in the presence of Gaussian noise. Consequently, differences in kurtosis between sand, silt-, and clay-like sediments are less pronounced compared to the equivalent fluid model.

CONCLUSIONS AND DISCUSSION

In this study, marine sediment is characterized by its elastic properties, including density, compressional and shear wave sound speeds, and attenuation. Variations in sediment properties lead to differences in sound pressure kurtosis. When shear rigidity is ignored, the equivalent fluid model can predict a similar trend for both time dispersion and kurtosis levels at 30 m and 300 m. However, at greater distances, incorporating a more realistic sediment description reveals notable variations in both time dispersion and kurtosis levels. For the pressure waveform, amplitude decreases at 3000 m. In terms of kurtosis, the current model predicts higher kurtosis levels at 3000 m for silt- and clay-like substrates. These results emphasize the importance of modeling sediment as an elastic medium when analyzing sound propagation over larger distances (above 3000 m), particularly for sediments containing silt and clay.

REFERENCES

Ainslie, MA (2010). "Principles of Sonar Performance Modeling ", *Praxis Books, Springer, Berlin*.

Ainslie, MA, Laws, RM and Sertlek, HÖ (2019). "EInternational Airgun Modeling Workshop: Validation of source signature and sound propagation models—Dublin (Ireland), July 16, 2016—problem description", *The IEEE Journal of Oceanic Engineering*, Vol 44, No 3, pp. 565–574.

Ainslie, MA, Laws, RM, Smith, MJ and MacGillivray, AO (2024). "Source and propagation modelling scenarios for environmental impact assessment: Model verification ", *The Journal of the Acoustical Society of America*, Vol 156, No 3, pp. 1489–1508.

ISO (2017). "ISO 18405:2017 Underwater acoustics—Terminology ", *International Organization for Standardization, Geneva*.

Lucke, K and MacGillivray, AO and Halvorsen, HB and Ainslie, MA and Zeddies, DG and Sisneros, JA (2024). "Recommendations on bioacoustical metrics relevant for regulating exposure to anthropogenic underwater sound ", *The Journal of the Acoustical Society of America*, Vol 156, No 4, pp. 2508–2526.

MacGillivray, AO and Chapman, NR (2012). "Modeling underwater sound propagation from an airgun array using the parabolic equation method ", *Canadian Acoustics - Acoustique canadienne*, Vol 40, No 1, pp. 19–25.

Müller, RAJ, von Benda-Beckmann, AM, Halvorsen, MB and Ainslie, MA (2020). "Application of kurtosis to underwater sound ", *The Journal of the Acoustical Society of America*, Vol 148, No 2, pp. 780–792.

Peng, Y, Tsouvalas, A, Stampoultzoglou, T and Metrikine, A (2021). "A fast computational model for near- and far-field noise prediction due to offshore pile driving ", *The Journal of the Acoustical Society of America*, Vol 149, No 3, pp. 1772–1790.

Sertlek, HÖ, Peng, Y, Ainslie, MA, von Benda-Beckmann, AM, Halvorsen, MB, Koessler, MW, Küsel, ET, MacGillivray, AO and Tsouvalas, A (2024). "Effects of sediment properties, distance from source, and frequency weighting on sound pressure and sound pressure kurtosis for marine airgun signatures", *The Journal of the Acoustical Society of America*, Vol 156, No 6, pp. 4242–4255.

Sidorovskaia, N and Li, K (2022). "Marine compressed air source array primary acoustic field characterization from at-sea measurements", *The Journal of the Acoustical Society of America*, Vol 151, No 6, pp. 3957–3978.

Slabbekoorn, H, Dalen, J, de Haan, D, Winter, HV, Radford, CA, Ainslie, MA, Heaney, KD, van Kooten, T, Thomas, L and Harwood, J (2019). "Population-level consequences of seismic surveys on fishes: An interdisciplinary challenge", *Fish Fish*, Vol. 20(4), pp. 653–685.

Southall, BL, Finneran, JJ, Reichmuth, CJ, Nachtigall, PE, Ketten, DR, Bowles, AE, Ellison, WT, Nowacek, DP and Tyack, PL (2019). "Marine mammal noise exposure criteria: Updated scientific recommendations for residual hearing effects ", *Aquatic Mammals*, Vol 45, No 2, pp. 125–232.